Decentralized Stability Certificates in IBR-Dominated Grids: The Role of the Network State

Zhimeng Wang†, Sushobhan Chatterjee†, Sijia Geng†, Richard Pates‡, Enrique Mallada†

***Abstract*—Small-signal instabilities, such as unforced sub-synchronous oscillations (SSOs), are increasingly observed in inverter-based resource (IBR) dominated grids. While decentralized stability certificates offer a scalable means to avoid instability onset, they are typically derived under restrictive network-state assumptions–such as small angle differences or negligible voltage drops–that cannot capture how departures from these conditions affect system stability. In this paper, we develop a network model and a decentralized analysis framework that explicitly characterizes how reactive power mismatches, line loading, and inverter control parameters jointly determine small-signal stability. We show that increased steady-state reactive power mismatches and line loading lead to more stringent conditions on admissible inverter droop gains. These results make decentralized stability certificates explicitly network-state dependent, showing how network stress shrinks the set of stabilizing local controller parameters.**

***Index Terms*—Decentralized stability, inverter-based resources, passivity, reactive power, small-signal stability.**

I. Introduction

Small-signal instabilities are becoming increasingly prevalent in inverter-based resource (IBR) dominated grids, often manifesting as unforced sub-synchronous oscillations (SSOs) [1]. Such instabilities have been reported across a wide range of scenarios, including weak-grid conditions, controller misconfigurations at commissioning, and post-contingency network reconfigurations [2], [3]. While some events can be explained by classical resonance phenomena or control-structure interactions [4], the precise mechanisms driving many of these oscillations remain poorly understood. In particular, instabilities often arise spontaneously, without a clear disturbance or topological trigger, underscoring the need for improved analytical tools that capture how the underlying network state shapes small-signal dynamics and stability-margins [5].

Recent research has emphasized the use of *decentralized certificates* to ensure small signal stability [6]–[11]. These approaches derive scale-free conditions that guarantee stability under bounded uncertainty, offering scalable alternatives to full electromagnetic transient (EMT) simulations and global eigenvalue analyses [6]. To obtain such tractable, decentralized conditions, most formulations either adopt simplifying network steady-state assumptions–such as small phase differences [7], [11], near-uniform voltage magnitudes [8], or active–reactive decoupling [6], [9]–or implicitly encode network-state dependence within the local linearization of inverter models [10]. As a result, the dependence of stability margins on the network state is either neglected, implicitly confined to a nominal regime, or absorbed into model abstractions.

In this paper, we develop a novel network model and accompanying analysis framework that derives decentralized stability certificates without imposing explicit or implicit assumptions on the network state. Our approach relies on a small-signal model in which lines and IBRs are represented as multi-port components, interconnected through an incidence-matrix-based network structure. In particular, each transmission line is modeled as a quasi-stationary multi-port subsystem mapping small deviations of nodal angles and voltages to directional real and reactive power flows, while inverter dynamics are represented through filtered droop gains. This explicit port-based decomposition makes the passivity properties of individual components–and potential violations thereof–transparent, enabling a systematic and decentralized application of loop transformation techniques to compensate for non-passive effects.

Applying this framework reveals an intrinsic coupling between the network steady state and the admissible control gains required for guaranteeing small-signal stability. In particular, our results show that increasing reactive power asymmetries ($Q_{ij} - Q_{ji}$) or line loading–captured through larger phase differences ($\theta_{ij} = \theta_i - \theta_j$)–progressively restrict the set of stabilizing voltage droop gains. These findings align with the well-established notion that small-signal stability depends on the operating point of the network, and indicate that decentralized certificates derived under nominal or lightly stressed conditions can be overly optimistic when applied to stressed operating regimes. Moreover, the derived conditions provide practical guidance for preserving stability by indicating when network-aware control retuning or operational redispatch may be required.

The rest of the paper is organized as follows. Section II reviews the preliminary tools used throughout the paper, including the passivity stability theorem and loop transformation techniques for analyzing feedback interconnections. Section III introduces the network and device models and describes their interconnection through a structured feedback representation. Section IV presents the main decentralized stability certificate and provides a detailed proof of the result. Section V demonstrates the implications of the proposed conditions through an illustrative numerical example. Finally, Section VI summarizes the main findings and discusses their implications for decentralized stability analysis and inverter-based grid operation.

II. Preliminaries

Our analysis relies on passivity theory and standard mechanisms for compensating the lack of passivity in interconnected

†Zhimeng Wang, Sushobhan Chatterjee, Sijia Geng, Enrique Mallada are with the Department of Electrical and Computer Engineering, Johns Hopkins University, Baltimore, MD, USA. Email: {zwang471, schatt21, sgeng, mallada}@jhu.edu

‡Richard Pates is with the Department of Automatic Control, Lund University, Lund, Sweden. Email: {richard.pates}@control.lth.se

systems. Here, we introduce passivity stability theorem, which provides sufficient conditions for the stability of feedback interconnections, and introduce loop transformation techniques that allow passivity properties to be modified through equivalent interconnection representations. These tools form the basis for the decentralized stability analysis developed in the remainder of the paper.

A. Internal Feedback Stability

We consider the standard negative feedback interconnection of two square, proper transfer matrices $H_1(s)$ and $H_2(s)$. The resulting closed-loop input–output relation can be written as

$$\begin{bmatrix} y_1 \\ y_2 \end{bmatrix} = \underbrace{\begin{bmatrix} (\mathbb{I}+H_1H_2)^{-1}H_1 & -(\mathbb{I}+H_1H_2)^{-1}H_1H_2 \\ H_2(\mathbb{I}+H_1H_2)^{-1}H_1 & H_2(\mathbb{I}+H_1H_2)^{-1} \end{bmatrix}}_{=:\, H_1 \# H_2(s)} \begin{bmatrix} u_1 \\ u_2 \end{bmatrix}, \tag{1}$$

where we use $\mathbb{I}$ as an identity matrix with proper dimensions, and $\mathbb{I}_m$ as an $m \times m$ identity matrix.

Definition 1 (Internal Feedback Stability)**.** *The negative feedback interconnection of $H_1(s)$, $H_2(s)$ is said to be* internally stable *if all transfer matrices comprising $H_1\#H_2(s)$ are stable, i.e., all poles of $H_1\#H_2(s)$ lie in the open left-half plane.*

Under the assumption that there are no right-half-plane pole–zero cancellations between $H_1(s)$ and $H_2(s)$—i.e., all right-half-plane poles of $H_1(s)$ and $H_2(s)$ are contained in the minimal realizations of $H_1(s)H_2(s)$ and $H_2(s)H_1(s)$—internal stability of one closed-loop transfer matrix implies internal stability of all others [12]. This notion will be used throughout the paper.

B. Passivity Stability Theorem

We briefly review standard passivity definitions and a classical passivity-based stability theorem for feedback interconnections.

Definition 2 (Passivity)**.** *A square, proper, real rational transfer matrix $H(s)$ is* passive *if:*

i. $H(s)$ has poles in $\Re(s) \leq 0$.

ii. The Hermitian part of $H(j\omega)$ is positive semidefinite for any ω for wich $j\omega$ is not a pole:

$$H(j\omega) + H^*(j\omega) \succeq 0.$$

iii. Any pole on the imaginary axis is simple, and its residue

$$R = \lim_{s \to j\omega_0} (s - j\omega_0)H(s)$$

is Hermitian positive semidefinite.

The transfer matrix is strictly passive *if inequalities in $i.$ and $ii.$ are strict.*

Theorem 1 (Feedback Stability via Passivity)**.** *Consider the standard negative feedback interconnection of two systems $H_1(s)$ and $H_2(s)$ with compatible dimensions. The closed-loop system is internally stable if the following conditions hold:*

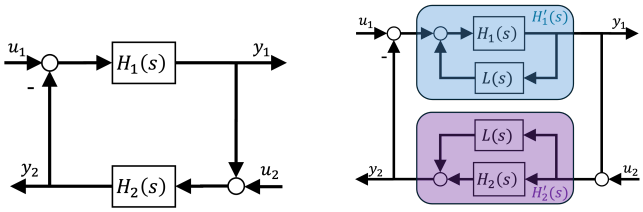

(a) Negative feedback interconnection of $H_1(s)$ and $H_2(s)$.

(b) Fig. 1a with loop transformation $L(s)$.

Fig. 1: Loop transformation.

i. System $H_1(s)$ is passive, and system $H_2(s)$ is strictly passive.

ii. The loop gain magnitude at infinite frequency satisfies the small-gain condition:

$$\bar{\sigma}\left(H_1(j\infty)\right)\bar{\sigma}\left(H_2(j\infty)\right) < 1.$$

Proof. The proof of this Theorem is standard. From completeness we provide a proof in Appendix A. □

C. Loop Transformation

We will use loop transformations to compensate the lack of passivity in transmission lines, allowing in this way to apply Theorem 1.

Lemma 1 (Simplified condition for internal stability [12])**.** *Consider a negative feedback interconnection of $H_1(s)$ and $H_2(s)$. Assume there are no RHP pole-zero cancellations between $H_1(s)$ and $H_2(s)$, i.e., all RHP poles in $H_1(s)$ and $H_2(s)$ are contained in the minimal realization of $H_1(s)H_2(s)$ and $H_2(s)H_1(s)$. Then, the negative feedback interconnection is internally feedback stable if and only if one of the four closed-loop transfer matrices is stable.*

Lemma 2 (Corollary 5.5 in [13])**.** *Suppose $H_1(s)$ is stable. Then the system in Fig. 1 is internally stable iff $(\mathbb{I}+H_2H_1)^{-1}H_2$ is stable.*

Theorem 2 (Loop transformation equivalence)**.** *Consider the interconnections in Fig. 1a and 1b. If there is no RHP pole-zero cancellation between $H_1(s)$ and $H_2(s)$, and $H_1(s)$ is stable, then the internal stability of the two systems are equivalent.*

Proof. See Appendix B. □

III. Network Model

In this section, we develop a first principle-based small-signal model of the IBRs and the transmission network, and then connect them to construct an interconnection.

A. Inverter-Based Resource (IBR) Model

We model each IBR as a grid-forming (GFM) device that regulates frequency through active power feedback and voltage magnitude through reactive power feedback. Let ΔP_i and ΔQ_i denote the incremental active and reactive power injected by inverter i into the network, and let $\Delta\omega_i$ and $\Delta \ln |v_i|$ denote

the incremental frequency and logarithmic voltage magnitude at bus i.

We adopt the standard sign convention in which positive power corresponds to injection into the grid, and the inverter control uses the *negative* of these quantities as feedback inputs. The small-signal inverter dynamics are modeled by

$$\begin{bmatrix}\Delta\omega_i\\ \Delta\ln|v_i|\end{bmatrix} = G_i(s)\begin{bmatrix}-\Delta P_i\\ -\Delta Q_i\end{bmatrix},$$

where the transfer matrix

$$G_i(s) := \begin{bmatrix}\frac{k_{p,i}}{\tau_{\omega,i}s+1} & 0\\ 0 & \frac{k_{q,i}}{\tau_{v,i}s+1}\end{bmatrix},$$

$k_{p,i}, k_{q,i} > 0$ are the active power–frequency droop gain and reactive power-voltage droop gain, respectively. $\tau_{\omega,i}, \tau_{v,i} > 0$ are the frequency and voltage control time constants, respectively.

We define

$$\begin{bmatrix}-\Delta P\\ -\Delta Q\end{bmatrix} := \begin{bmatrix}-\Delta P_1\\ -\Delta Q_1\\ \vdots\\ -\Delta P_n\\ -\Delta Q_n\end{bmatrix} \in \mathbb{R}^{2n}, \begin{bmatrix}\Delta\omega\\ \Delta\ln|v|\end{bmatrix} := \begin{bmatrix}\Delta\omega_1\\ \Delta\ln|v_1|\\ \vdots\\ \Delta\omega_n\\ \Delta\ln|v_n|\end{bmatrix} \in \mathbb{R}^{2n}$$

as the input and output signals of the IBR devices. Thus the dynamics of all the inverters concatenated is characterized by

$$\begin{bmatrix}\Delta\omega\\ \Delta\ln|v|\end{bmatrix} = G(s)\begin{bmatrix}-\Delta P\\ -\Delta Q\end{bmatrix}, \tag{2}$$

where $G(s) = \mathrm{blkdiag}\,(G_1(s), \cdots, G_n(s))$.

B. Line Model

Consider a lossless transmission line $e = \{i, j\}$ connecting buses i and j. Let

$$v_i = |v_i|e^{j\theta_i}, \qquad v_j = |v_j|e^{j\theta_j}, \qquad \theta_{ij} := \theta_i - \theta_j$$

denote the steady-state voltage phasors and phase difference. The line is modeled as purely inductive with inductance L_e, and we define the normalized susceptance $b_e := \frac{1}{\omega_0 L_e}$, where ω_0 is the synchronous angular frequency.

The steady-state complex power injected from bus i into the line is

$$S_{ij} := P_{ij} + jQ_{ij} = v_i\, i_{ij}^*,$$

with $i_{ij} = jb_e(v_i - v_j)$, and S_{ji} defined analogously.

Linearizing the AC power-flow equations around the operating point yields a quasi-stationary, port-based small-signal model of the line,

$$\begin{bmatrix}\Delta P_{ij}\\ \Delta Q_{ij}\\ \Delta P_{ji}\\ \Delta Q_{ji}\end{bmatrix} = N_e(s)\begin{bmatrix}\Delta\omega_i\\ \Delta\ln|v_i|\\ \Delta\omega_j\\ \Delta\ln|v_j|\end{bmatrix},$$

where the line transfer matrix admits the factorization

$$N_e(s) = J_e\,\mathrm{diag}\left(\frac{1}{s},\, 1,\, \frac{1}{s},\, 1\right).$$

We use $I_n(s) = \mathrm{diag}\left(\frac{1}{s}, 1, \ldots, \frac{1}{s}, 1\right) \in \mathbb{C}^{n\times n}$, thus $N_e(s) = J_e I_4(s)$. The integrator terms arise from the kinematic relation $\dot\theta_k = \omega_k$, while the static gain matrix $J_e := b_e|v_i||v_j|\,\bar J_e$ captures the steady-state sensitivity of line power flows to voltage magnitudes and phase differences, and the normalized Jacobian $\bar J_e \in \mathbb{R}^{4\times4}$ is given by

$$\bar J_e = \begin{bmatrix}\cos\theta_{ij} & \sin\theta_{ij} & -\cos\theta_{ij} & \sin\theta_{ij}\\ \sin\theta_{ij} & 2\frac{|v_i|}{|v_j|} - \cos\theta_{ij} & -\sin\theta_{ij} & -\cos\theta_{ij}\\ -\cos\theta_{ij} & -\sin\theta_{ij} & \cos\theta_{ij} & -\sin\theta_{ij}\\ \sin\theta_{ij} & -\cos\theta_{ij} & -\sin\theta_{ij} & 2\frac{|v_j|}{|v_i|} - \cos\theta_{ij}\end{bmatrix}.$$

Let $E = \{e_1, \ldots, e_m\}$ denote the set of transmission lines. Stacking the incremental nodal variables and line power flows over all lines, we define

$$\begin{bmatrix}\Delta\omega_E\\ \Delta\ln|v_E|\end{bmatrix} := \begin{bmatrix}\Delta\omega_{i_1}\\ \Delta\ln|v_{i_1}|\\ \Delta\omega_{j_1}\\ \Delta\ln|v_{j_1}|\\ \vdots\\ \Delta\omega_{i_m}\\ \Delta\ln|v_{i_m}|\\ \Delta\omega_{j_m}\\ \Delta\ln|v_{j_m}|\end{bmatrix}, \qquad \begin{bmatrix}\Delta P_E\\ \Delta Q_E\end{bmatrix} := \begin{bmatrix}\Delta P_{i_1j_1}\\ \Delta Q_{i_1j_1}\\ \Delta P_{j_1i_1}\\ \Delta Q_{j_1i_1}\\ \vdots\\ \Delta P_{i_mj_m}\\ \Delta Q_{i_mj_m}\\ \Delta P_{j_mi_m}\\ \Delta Q_{j_mi_m}\end{bmatrix}.$$

The concatenated line dynamics can then be written compactly as

$$\begin{bmatrix}\Delta P_E\\ \Delta Q_E\end{bmatrix} = N_E(s)\begin{bmatrix}\Delta\omega_E\\ \Delta\ln|v_E|\end{bmatrix}, \tag{3}$$

where

$$N_E(s) = \mathrm{blkdiag}(N_{e_1}(s), \ldots, N_{e_m}(s)) = J_E\, I_{4m}(s),$$

with $J_E := \mathrm{blkdiag}(J_{e_1}, \ldots, J_{e_m})$.

C. Interconnection Model

To connect the bus vector signals and the line-end vector signals, we introduce the matrix

$$M := \begin{bmatrix}M_{e_1} & M_{e_2} & \cdots & M_{e_m}\end{bmatrix} \in \{0,1\}^{2n\times4m},$$

where for each line,

$$M_e = \begin{bmatrix}e_i & e_j\end{bmatrix} \otimes \mathbb{I}_2 \in \{0,1\}^{2n\times4},$$

and e_k is the k-th standard basis vector.

Therefore, the bus vector signals and the line-end vector signals can be related as

$$\begin{bmatrix}\Delta\omega_E\\ \Delta\ln|v_E|\end{bmatrix} = M^\top\begin{bmatrix}\Delta\omega\\ \Delta\ln|v|\end{bmatrix}, \quad \begin{bmatrix}\Delta P\\ \Delta Q\end{bmatrix} = M\begin{bmatrix}\Delta P_E\\ \Delta Q_E\end{bmatrix} \tag{4}$$

Equations (2), (3), and (4) provide a compact first-principles description of the full networked system, in which the inverter dynamics and the line dynamics are interconnected exclusively through the operators $M^\top$ (node-to-edge) and M (edge-to-node). We denote this interconnection between systems G and N_E via M and $M^\top$ as $G\#_M N_E$. This structure will be the basis for the passivity and stability analysis in the sequel.

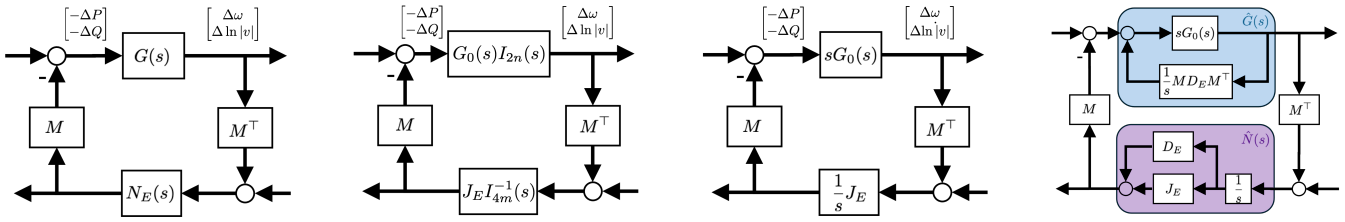

(a) System $G(s)\#_M N_E(s)$. (b) $G_0(s)I_{2n}(s)\#_M J_E I_{4m}^{-1}(s)$. (c) System $sG_0(s)\#_M \frac{1}{s}J_E$. (d) System $\hat{G}(s)\#_M \hat{N}(s)$.

Fig. 2: Systems for stability analysis.

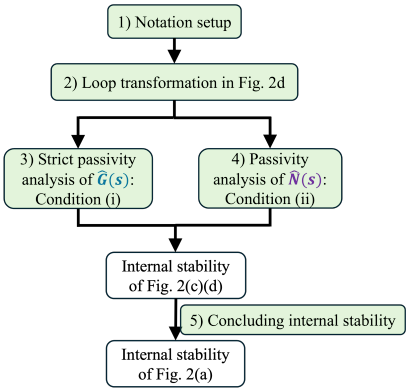

Fig. 3: Flow chart of the proof of Theorem 3. The colored blocks represent the steps.

IV. Decentralized Stability Certificate

We now present and prove the main result of this paper.

A. Main Result

Theorem 3 (Decentralized Stability Certificate)**.** *Consider the device and network models in* (2)*,* (3)*, and* (4)*, interconnected as $G(s)\#_M N_E(s)$ in Fig. 2a. If the following condition holds: For each line $e=\{i,j\}\in E$,*

$$\left(2\frac{d_e}{b_e|v_i||v_j|}-\frac{2}{\cos\theta_{ij}}\right)\sqrt{\left(\frac{Q_{ij}-Q_{ji}}{b_e|v_i||v_j|}\right)^2+4} + \left(\frac{d_e}{b_e|v_i||v_j|}\right)^2-\frac{2}{\cos\theta_{ij}}\frac{d_e}{b_e|v_i||v_j|}+4\geq 0, \tag{5}$$

where $\sum_{e:i\in e} d_e = \frac{1}{k_{q,i}}$. Then $G(s)\#_M N_E(s)$ is internally stable.

B. Proof of Main Theorem

We prove Theorem 3 by following the flow chart in Fig. 3.

1) Notation setup: To facilitate the stability analysis, we normalize the system parameters around the operating point. We define the operating angle coefficients $c:=\cos\theta_{ij}, s:=\sin\theta_{ij}$. Furthermore, we introduce the normalized gain and the corresponding diagonal matrix

$$\bar{d}_e := \frac{d_e}{b_e|v_i||v_j|}, \quad \bar{D}_e = \mathrm{diag}(0,\bar{d}_e,0,\bar{d}_e),$$

to be used in our loop transformation, and the normalized reactive power flow p_{ij}, q_{ij} and q_{ji}

$$p_{ij}:=\frac{P_{ij}}{b_e|v_i||v_j|}, \qquad q_{ij}:=\frac{Q_{ij}}{b_e|v_i||v_j|}, \qquad q_{ji}:=\frac{Q_{ji}}{b_e|v_i||v_j|}.$$

Also notice the standard power-flow identities of lossless lines

$$p_{ij}=\sin\theta_{ij}=s, \qquad q_{ij}-q_{ji}=\frac{Q_{ij}-Q_{ji}}{b|v_i||v_j|}=\frac{|v_i|}{|v_j|}-\frac{|v_j|}{|v_i|}.$$

We will prove our results using the following coordinates

$$\Sigma := \frac{|v_i|}{|v_j|}+\frac{|v_j|}{|v_i|}+\bar{d}_e=\sqrt{(q_{ij}-q_{ji})^2+4}+\bar{d}_e, \tag{6}$$

$$\Delta := \frac{|v_i|}{|v_j|}-\frac{|v_j|}{|v_i|}=q_{ij}-q_{ji}. \tag{7}$$

2) Loop transformation: The map in (3) is in general not passive, as J_E is in general not positive semidefinite. To facilitate the subsequent analysis, we consider the systems in Fig. 2, in which Fig. 2a is the original system, and can be equivalently expressed as in Fig. 2b, where

$$G_0(s)=\mathrm{blkdiag}\left(\begin{bmatrix}\frac{k_{p,i}}{s(\tau_{\omega,i}s+1)} & 0\\ 0 & \frac{k_{q,i}}{\tau_{v,i}s+1}\end{bmatrix}\right),$$

and $G_0(s)$ characterizes the dynamics

$$\begin{bmatrix}\Delta\theta\\ \Delta\ln|v|\end{bmatrix}=G_0(s)\begin{bmatrix}-\Delta P\\ -\Delta Q\end{bmatrix}.$$

In Fig. 2c, $G'(s):=sG_0(s)$ characterizes the dynamics

$$\begin{bmatrix}\Delta\omega\\ \Delta\dot{\ln}|v|\end{bmatrix}=G'(s)\begin{bmatrix}-\Delta P\\ -\Delta Q\end{bmatrix}. \tag{8}$$

For each $e=\{i,j\}$, we choose loop shifting parameter $d_e\geq 0$, and apply the corresponding loop shifting matrix D_E to the line dynamics in Fig. 2c, which yields the loop shifted interconnection in Fig. 2d. On the IBR side, this loop transformation induces the additional nodal positive feedback $\frac{1}{s}K\begin{bmatrix}\Delta\omega\\ \Delta\dot{\ln}|v|\end{bmatrix}$, where $K:=M\,D_E\,M^\top$. By construction, K is diagonal and acts only on the voltage-magnitude channels:

$$K=\mathrm{diag}(0,\kappa_1,0,\kappa_2,\ldots,0,\kappa_n),$$

where $\kappa_i=\sum_{e:i\in e} d_e$. Note that D_e acts locally on each line, whereas K aggregates these effects at the nodal level.

3) Strict passivity analysis of loop shifted devices $\hat{G}(s)$: The diagonal term $\frac{1}{s}K$ is equivalent to introducing, at each bus i, a local positive feedback in the $\ln|v_i|$ channel with gain κ_i.

Given the IBR dynamics in (8), the additional feedback κ_i/s acts as a positive feedback around the first-order system $\frac{k_{q,i}s}{\tau_{v,i}s+1}$ in the voltage channel. Consequently, the effective voltage-channel dynamics become

$$\frac{k_{q,i}s}{\tau_{v,i}s+1-\kappa_i k_{q,i}},$$

which remains *strictly* passive with $\kappa_i = \frac{1}{k_{q,i}}$.

4) Passivity analysis of loop shifted lines $\hat{N}(s)$: With the loop transformation introduced, each of the line transfer function $\frac{1}{s}J_e$ can be replaced by the shifted map

$$\frac{1}{s}J_e \;=\; \frac{1}{s}(J_e+D_e) \;-\; \frac{1}{s}D_e.$$

Equivalently, we define the *passivized* line block

$$\bar{N}_{\ln,e}(s) := \frac{1}{s}\,(J_e+D_e), \qquad N_{D,e}(s) := \frac{1}{s}\,D_e,$$

so that the original line is decomposed into a passive candidate $\bar{N}_{\ln,e}$ and a diagonal integrator $N_{D,e}$. Since $\frac{1}{s}$ is positive real, a sufficient condition for $\bar{N}_{\ln,e}(s)$ to be passive is $\bar{J}_e+\bar{D}_e \succeq 0$, and is a simple semidefinite condition on d_e.

Stacking over all lines gives the passivized stacked line map

$$\bar{N}_{\ln}(s) = \frac{1}{s}\,(J_E+D_E), \qquad N_D(s) = \frac{1}{s}\,D_E.$$

For each line, define

$$H_e := \bar{J}_e+\bar{D}_e = \begin{bmatrix} c & s & -c & s \\ s & 2\frac{|v_i|}{|v_j|}-c+\bar{d}_e & -s & -c \\ -c & -s & c & -s \\ s & -c & -s & 2\frac{|v_j|}{|v_i|}-c+\bar{d}_e \end{bmatrix}. \quad (9)$$

The definition in (6)–(7) can be equivalently written as

$$2\frac{|v_i|}{|v_j|}+\bar{d}_e = \Sigma+\Delta, \qquad 2\frac{|v_j|}{|v_i|}+\bar{d}_e = \Sigma-\Delta.$$

To analyze the definiteness of H_e, we apply a congruence transformation $\tilde{H}_e := T^\top H_e T$ that transforms the basis into Σ and Δ, thereby block-diagonalizing the matrix and simplifying the stability check. We pick

$$T := \begin{bmatrix} 1 & 0 & 1 & 0 \\ 0 & 1 & 0 & 1 \\ 1 & 0 & -1 & 0 \\ 0 & 1 & 0 & -1 \end{bmatrix}.$$

Applying the transformation to (9) and simplifying yields

$$\tilde{H}_e = \begin{bmatrix} 0 & 0 & 0 & 0 \\ 0 & 2\Sigma-4c & 4s & 2\Delta \\ 0 & 4s & 4c & 0 \\ 0 & 2\Delta & 0 & 2\Sigma \end{bmatrix},$$

thus $H_e \succeq 0$ is equivalent to $G_e \succeq 0$, and is further equivalent to $\hat{G}_e := \frac{1}{2}G_e \succeq 0$, where

$$G_e := \begin{bmatrix} 2\Sigma-4c & 4s & 2\Delta \\ 4s & 4c & 0 \\ 2\Delta & 0 & 2\Sigma \end{bmatrix}, \hat{G}_e = \begin{bmatrix} \Sigma-2c & 2s & \Delta \\ 2s & 2c & 0 \\ \Delta & 0 & \Sigma \end{bmatrix} \succeq 0.$$

We assume $c>0$, so the middle diagonal entry $2c$ is strictly positive. Then $\hat{G}_e \succeq 0$ is equivalent to the Schur complement of the middle block being PSD:

$$S_e := \begin{bmatrix} \Sigma-2c & \Delta \\ \Delta & \Sigma \end{bmatrix} - \frac{1}{2c}\begin{bmatrix} 2s \\ 0 \end{bmatrix}\begin{bmatrix} 2s & 0 \end{bmatrix} = \begin{bmatrix} \Sigma-2c-\dfrac{2s^2}{c} & \Delta \\ \Delta & \Sigma \end{bmatrix},$$

it is PSD iff its diagonals and determinant are nonnegative.

We substitute Σ and Δ into (5), thus the condition ensures

$$-\Delta^2+\Sigma^2-\frac{2\Sigma}{c} = \Sigma^2-2c\Sigma-\frac{2s^2}{c}\Sigma-\Delta^2 = \det(S_e) \geq 0 \quad (10)$$

Moreover, (10) guarantees

$$\Sigma^2-\frac{2}{c}\Sigma \geq \Delta^2 \geq 0 \;\Rightarrow\; \Sigma\left(\Sigma-\frac{2}{c}\right) \geq 0.$$

Since $\Sigma \geq 0$, this implies $\Sigma \geq \frac{2}{c}$, i.e., (10) implies the smallest diagonal element in S_e is nonnegative.

In conclusion, the condition ensures S_e is PSD, implying that $\hat{G}_e$, G_e and H_e are PSD, which further implies the passivity of the loop-shifted lines.

5) Concluding internal stability: Given that conditions (i)–(ii) ensure the strict passivity of the loop shifted IBRs and the passivity of the loop shifted lines, the loop-shifted system $\hat{G}(s)\#_M\hat{N}(s)$ in Fig. 2d is internally stable. Since $sG_0(s)$ is stable and there is no RHP pole-zero cancellation between $sG_0(s)$ and $\frac{1}{s}J_E$, we apply Theorem 2 and conclude that system $sG_0(s)\#_M\frac{1}{s}J_E$ is also internally stable, i.e., signals $(\Delta P, \Delta Q, \Delta\omega, \Delta\ln|v|) \to 0$ as $t\to\infty$. To further show that $\Delta\ln|v| \to 0$ as $t\to\infty$, which can be implied by the internal stability of the original system $G(s)\#_M N_E(s)$ in Fig. 2a, we adapt the proof method from [11] and state the following.

Lemma 3. *Consider system $G(s)\#_M N_E(s)$ in Fig. 2a, and system $\hat{G}(s)\#_M\hat{N}(s)$ in Fig. 2d. Then, internal feedback stability of the minimal realization of all four closed-loop transfer functions of the loop-shifted system $\hat{G}(s)\#_M\hat{N}(s)$ implies internal feedback stability of $G(s)\#_M N_E(s)$.*

Proof. See Appendix C. □

V. Numerical Example

We consider a two-bus system composed of two GFM inverters interconnected by a single transmission line. To validate the proposed stability certificates, we adopt a third-order nonlinear GFM model, as detailed in Appendix D, whose linearization yields (2). We begin by linearizing the nonlinear dynamics around a stable equilibrium point obtained with the following parameter settings: $p_1^* = -4$ p.u., $p_2^* = 4$ p.u., $q_1^* = 1.2$ p.u., $q_2^* = 0.5$ p.u., $k_{p,1} = k_{p,2} = 1.8$ p.u., $k_{q,1} = k_{q,2} = 0.3$ p.u., and $\omega_b = 120\pi$ rad/s. These parameters are selected to represent an operating condition characterized by voltage mismatch and line loading, as summarized below.

- Grid State: $|v_1| = 1.0218$ p.u., $|v_2| = 0.9919$ p.u., and phase angle $\theta_1 = 0°$, $\theta_2 = 23.2448°$.
- Line Parameter: $b_e = 10.0$ p.u.
- Control Gains: $k_{q,1} = k_{q,2} = 0.3$.

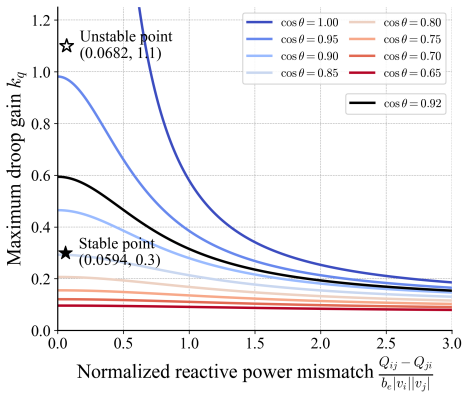

Fig. 4: $\cos\theta$ level sets illustrating how the maximum droop gain varies with $\frac{Q_{ij}-Q_{ji}}{b_e|v_i||v_j|}$. For each level set, the stable region encloses the origin.

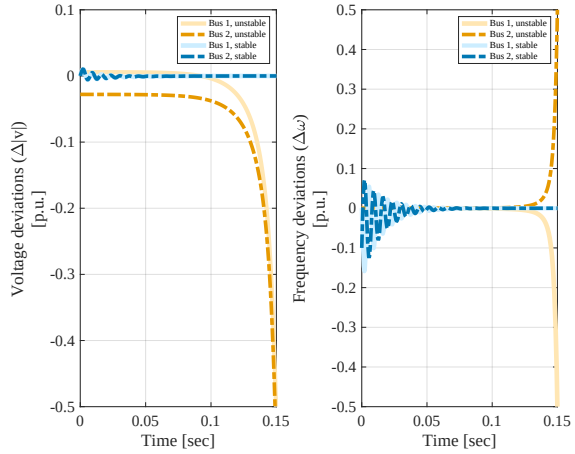

Fig. 5: Dynamic response of the 2-bus system considering one stable and one unstable scenario.

From the above, there is $\cos\theta = 0.9188$, $\frac{Q_{ij}-Q_{ji}}{b_e|v_1||v_2|} = 0.0593$. One can verify that, with $\kappa_i = \sum_{e:i\in e} d_e = \frac{1}{k_{q,i}}$, the condition is satisfied.

In Fig. 4, we plot the maximum admissible droop gain to maintain stability versus the $\frac{Q_{ij}-Q_{ji}}{b_e|v_i||v_j|}$. The region below each curve represents the stable operating set for a given $\cos\theta$. The varying curves represent different $\cos\theta$ values. We observe a clear inverse relationship between the reactive power mismatch and the stability margin. As the mismatch increases, the maximum allowable droop gain decreases monotonically. Furthermore, the system stability margins degrades significantly with smaller $\cos\theta$. This indicates that operating points with high reactive loading and large voltage disparity require much more conservative controller tuning to ensure stability. To validate our numerical example, in Fig. 4, we highlight the stability boundary for $\cos\theta = 0.92$ and the operating point from the example with a "★". Since the operating point lies within the safe region, the system is confirmed to be stable.

Furthermore, we examine an alternative operating point obtained by setting $k_{q,1} = 1.1$ p.u., and $k_{q,2} = 1$ p.u., while keeping all other parameters unchanged. This operating point is marked with a "☆" in Fig. 4, and violates the stability conditions established in Theorem 3, thereby demonstrating the ability of the proposed certificates to correctly characterize its stability properties. Fig. 5 presents time-domain simulations that corroborate the theoretical analysis for both the stable and unstable operating points. The left panel depicts the voltage deviations, whereas the right panel illustrates the frequency synchronization dynamics. This confirms that the proposed decentralized certificate is sufficient to guarantee the dissipation of oscillation energy.

VI. Conclusion

In this paper, we present a decentralized method for certifying the small-signal stability of IBR-dominated grids, with a specific focus on the impact of reactive power flows. We demonstrate that the network's operating point is an active factor in determining local passivity. By passivizing both devices and lines using loop transformation, we derive stability criteria that are both rigorous and practically implementable. These findings offer a clearer path towards "plug-and-play" integration of IBRs, ensuring robust operation even as grid complexity and interactions increase.

VII. AI Usage Disclosure

The authors used AI tools to assist with narrative polishing, including spell-checking, visualization coding and debugging. None of the narrative was directly produced by AI; it was used solely in an advisory role and did not replace the authors. All models and ideas are the sole intellectual property of the authors, and no AI model contributed to their development.

References

[1] L. Fan, Z. Miao, S. Shah, Y. Cheng, J. Rose, S.-H. Huang, B. Pal, X. Xie, N. Modi, S. Wang, *et al.*, "Real-world 20-hz ibr subsynchronous oscillations: Signatures and mechanism analysis," *IEEE Transactions on Energy Conversion*, vol. 37, no. 4, pp. 2863–2873, 2022.

[2] Y. Li, L. Fan, and Z. Miao, "Wind in weak grids: Low-frequency oscillations, subsynchronous oscillations, and torsional interactions," *IEEE Transactions on Power Systems*, vol. 35, no. 1, pp. 109–118, 2019.

[3] R. N. Damas, Y. Son, M. Yoon, S.-Y. Kim, and S. Choi, "Subsynchronous oscillation and advanced analysis: A review," *IEEE Access*, vol. 8, pp. 224020–224032, 2020.

[4] J. Shair, X. Xie, L. Wang, W. Liu, J. He, and H. Liu, "Overview of emerging subsynchronous oscillations in practical wind power systems," *Renewable and Sustainable Energy Reviews*, vol. 99, pp. 159–168, 2019.

[5] Y. Cheng, L. Fan, J. Rose, S.-H. Huang, J. Schmall, X. Wang, X. Xie, J. Shair, J. R. Ramamurthy, N. Modi, *et al.*, "Real-world subsynchronous oscillation events in power grids with high penetrations of inverter-based resources," *IEEE Transactions on Power Systems*, vol. 38, no. 1, pp. 316–330, 2022.

[6] R. Pates and E. Mallada, "Robust scale-free synthesis for frequency control in power systems," *IEEE Transactions on Control of Network Systems*, vol. 6, no. 3, pp. 1174–1184, 2019.

[7] P. Vorobev, S. Chevalier, and K. Turitsyn, "Decentralized stability rules for microgrids," in *2019 American Control Conference (ACC)*, pp. 2596–2601, IEEE, 2019.

[8] J. D. Watson and I. Lestas, "Control of interlinking converters in hybrid ac/dc grids: Network stability and scalability," *IEEE Transactions on Power Systems*, 2020.

[9] Z. Siahaan, E. Mallada, and S. Geng, "Decentralized stability criteria for grid-forming control in inverter-based power systems," in *2024 IEEE Power & Energy Society General Meeting (PESGM)*, pp. 1–5, IEEE, 2024.

[10] L. Huang, D. Wang, X. Wang, H. Xin, P. Ju, K. H. Johansson, and F. Dörfler, "Gain and phase: Decentralized stability conditions for power electronics-dominated power systems," *IEEE Transactions on Power Systems*, vol. 39, no. 6, pp. 7240–7256, 2024.
[11] V. Häberle, X. He, L. Huang, F. Dörfler, and S. Low, "Decentralized parametric stability certificates for grid-forming converter control," *arXiv preprint arXiv:2503.05403*, 2025.
[12] S. Skogestad and I. Postlethwaite, *Multivariable feedback control: analysis and design*. john Wiley & sons, 2005.
[13] K. Zhou, J. Doyle, and K. Glover, *Robust and optimal control*. Prentice Hall, 1996.

APPENDIX

A. Proof of Theorem 1

The internal stability of the feedback system in Fig. 1a is characterized by the following:

$$\begin{bmatrix} (\mathbb{I}+H_2H_1)^{-1} & (\mathbb{I}+H_2H_1)^{-1}H_2 \\ H_1(\mathbb{I}+H_2H_1)^{-1} & H_1(\mathbb{I}+H_2H_1)^{-1}H_2 \end{bmatrix}. \tag{11}$$

Given the strict passivity of H_2, it suffices to only check the stability of $H_1(\mathbb{I}+H_2H_1)^{-1}$ [13], which is equivalent to $-1 \notin \sigma(H_2H_1)$.[1] Suppose $-1 \in \sigma(H_2H_1)$, let $v \neq \vec{0}$ be the corresponding eigenvector. Thus $-v = H_2H_1v$. It follows that

$$-v^*H_1^*v = v^*H_1^*H_2H_1v. \tag{12}$$

We take the conjugate transpose of both sides, it yields

$$-v^*H_1v = v^*H_1^*H_2^*H_1v. \tag{13}$$

Summing both sides of (12) and (13) gives

$$-v^*(H_1+H_1^*)v = v^*H_1^*(H_2+H_2^*)H_1v. \tag{14}$$

By the passivity of H_1 and strict passivity of H_2, the left hand side of (14) is nonpositive, while the right hand side is strictly positive for $v \neq \vec{0}$. Thus there is contradiction, indicating that $-1 \notin \sigma(H_2H_1)$, and that the interconnection is internally stable given the conditions in Theorem 1.

B. Proof of Theorem 2

Given Lemma 1 and Lemma 2, the internal stability of the two interconnections can be guaranteed by one transfer matrix in the 2×2 block transfer matrix in (11). Check the transfer functions from u_1 to y_1 for Fig. 1b first.

$$\begin{aligned}
&\left(\mathbb{I}+H_1'H_2'\right)^{-1}H_1' \\
=&\left[\mathbb{I}+H_1(\mathbb{I}-LH_1)^{-1}(H_2+L)\right]^{-1}H_1(\mathbb{I}-LH_1)^{-1} \\
=&\left[\mathbb{I}+H_1(\mathbb{I}-LH_1)^{-1}H_2+H_1(\mathbb{I}-LH_1)^{-1}L\right]^{-1}H_1(\mathbb{I}-LH_1)^{-1} \\
=&\left[\mathbb{I}+H_1(\mathbb{I}-LH_1)^{-1}H_2+(\mathbb{I}-H_1L)^{-1}H_1L\right]^{-1}H_1(\mathbb{I}-LH_1)^{-1} \\
=&\left[(\mathbb{I}-H_1L)^{-1}(\mathbb{I}-H_1L+H_1L)+H_1(\mathbb{I}-LH_1)^{-1}H_2\right]^{-1}H_1(\mathbb{I}-LH_1)^{-1} \\
=&\left[(\mathbb{I}-H_1L)^{-1}+H_1(\mathbb{I}-LH_1)^{-1}H_2\right]^{-1}H_1(\mathbb{I}-LH_1)^{-1} \\
=&\left[(\mathbb{I}-H_1L)^{-1}+(\mathbb{I}-H_1L)^{-1}H_1H_2\right]^{-1}H_1(\mathbb{I}-LH_1)^{-1} \\
=&\left[(\mathbb{I}-H_1L)^{-1}(\mathbb{I}+H_1H_2)\right]^{-1}H_1(\mathbb{I}-LH_1)^{-1} \\
=&(\mathbb{I}+H_1H_2)^{-1}H_1
\end{aligned}$$

The last expression $(\mathbb{I}+H_1(s)H_2(s))^{-1}H_1(s)$ is precisely the transfer function from u_1 to y_1 in Fig. 1a. Thus the transfer functions are equivalent, implying the equivalence of internal stability between system $H_1(s)\#H_2(s)$ in Fig. 1a and system $H_1'(s)\#H_2'(s)$ in Fig. 1b.

[1]Here $\sigma(A)$ represents the set of eigenvalues of A.

C. Proof of Lemma 3

Since $sG_0(s)$ is stable and there is no RHP pole-zero cancellation between $sG_0(s)$ and $\frac{1}{s}J_E$, we apply Theorem 2 and conclude that system $sG_0(s)\#_M\frac{1}{s}J_E$ is also internally stable. Moreover, notice that

$$\left(\mathbb{I}+G'\frac{1}{s}J_E\right)^{-1}G' = \mathrm{diag}(1,s,\cdots,1,s)\cdot(\mathbb{I}+GN_E)^{-1}G,$$

thus we can conclude the stability of $(\mathbb{I}+GN_E)^{-1}G$ if the step response of the voltage derivatives converges to zero, i.e.,

$$\lim_{s\to 0} s\frac{1}{s}\left(\mathbb{I}+G'\frac{1}{s}J_E\right)^{-1}G' = \mathbb{I}\otimes\begin{bmatrix}* & 0\\ 0 & 0\end{bmatrix}. \tag{15}$$

To show (15), first simplify it as

$$\lim_{s\to 0}\left(\mathbb{I}+G'\frac{1}{s}J_E\right)^{-1}G' = \mathbb{I}\otimes\begin{bmatrix}* & 0\\ 0 & 0\end{bmatrix}.$$

We define permutation matrix

$$\mathcal{P} = \begin{bmatrix}\mathcal{P}_u\\ \hline \mathcal{P}_l\end{bmatrix} \in \{0,1\}^{2n\times 2n},$$

where

$$(\mathcal{P}_u)_{i,j} = \begin{cases}1 & \text{if } j = 2i-1\\ 0 & \text{otherwise}\end{cases}, \quad (\mathcal{P}_l)_{i,j} = \begin{cases}1 & \text{if } j = 2i\\ 0 & \text{otherwise}\end{cases}.$$

We apply the permutation matrix $\mathcal{P}$ to the limit we want to show,

$$\lim_{s\to 0}\mathcal{P}\left(\mathbb{I}+G'\frac{1}{s}J_E\right)^{-1}G'\mathcal{P}^\top = \mathcal{P}\mathbb{I}\otimes\begin{bmatrix}* & 0\\ 0 & 0\end{bmatrix}\mathcal{P}^\top = \begin{bmatrix}* & 0\\ 0 & 0\end{bmatrix}. \tag{16}$$

Due to the orthogonality of $\mathcal{P}$, the LHS of (16) is equivalent to

$$\lim_{s\to 0}(\mathbb{I}+G^\pi N^\pi)^{-1}G^\pi, \tag{17}$$

where

$$\begin{aligned}
G^\pi =& \mathcal{P}G'\mathcal{P}^\top = \begin{bmatrix}\mathrm{diag}\left(\frac{k_{p,i}}{\tau_{\omega,i}s+1}\right) & 0\\ 0 & \mathrm{diag}\left(\frac{k_{q,i}s}{\tau_{v,i}s+1}\right)\end{bmatrix}\\
N^\pi =& \frac{1}{s}\mathcal{P}J_E\mathcal{P}^\top.
\end{aligned}$$

Notice that N^π contains a $1/s$ factor. We define $K^\pi = sN^\pi$ and take the limits:

$$\lim_{s\to 0}G^\pi = \begin{bmatrix}\mathrm{diag}(k_{p,i}) & 0\\ 0 & 0\end{bmatrix} := \bar{G},$$

$$\lim_{s\to 0}sN^\pi = \begin{bmatrix}K_{11} & K_{12}\\ K_{21} & K_{22}\end{bmatrix} := K^\pi.$$

Thus, substituting $(\mathbb{I}+G^\pi N^\pi)^{-1} = s(s\mathbb{I}+G^\pi K^\pi)^{-1}$, (17) becomes

$$\begin{aligned}
&\lim_{s\to 0} s\left(s\mathbb{I}+\bar{G}K^\pi\right)^{-1}\bar{G}\\
=&\lim_{s\to 0} s\begin{bmatrix}s\mathbb{I}+\mathrm{diag}(k_{p,i})K_{11} & \mathrm{diag}(k_{p,i})K_{12}\\ 0 & s\mathbb{I}\end{bmatrix}^{-1}\begin{bmatrix}\mathrm{diag}(k_{p,i}) & 0\\ 0 & 0\end{bmatrix}\\
=&\lim_{s\to 0} s\begin{bmatrix}(s\mathbb{I}+\mathrm{diag}(k_{p,i})K_{11})^{-1} & \star\\ 0 & \frac{1}{s}\mathbb{I}\end{bmatrix}\begin{bmatrix}\mathrm{diag}(k_{p,i}) & 0\\ 0 & 0\end{bmatrix}\\
=&\lim_{s\to 0}\begin{bmatrix}s\,(s\mathbb{I}+\mathrm{diag}(k_{p,i})K_{11})^{-1}\,\mathrm{diag}(k_{p,i}) & 0\\ 0 & 0\end{bmatrix}
\end{aligned}$$

which yields the required structure.

D. GFM Modeling Equations

The nonlinear differential-algebraic equations (DAEs) describing the GFM dynamics are given below in per units. The notation for variables and parameters is explained herein.

1) Differential Equations:

$$\begin{aligned}\dot{\theta} &= \omega_b \delta\omega \\ \tau_\omega \dot{\delta\omega} &= -\delta\omega + (p^* - p)k_p \\ \tau_v \dot{\delta|v|} &= -\delta|v| + (q^* - q)k_q\end{aligned}$$

2) Algebraic Equations:

$$\begin{aligned}\delta\omega &= \omega - \omega_0 \\ \delta|v| &= |v| - |v_0| \\ p &= v_\mathrm{D} i_\mathrm{D} + v_\mathrm{Q} i_\mathrm{Q} \\ q &= v_\mathrm{Q} i_\mathrm{D} - v_\mathrm{D} i_\mathrm{Q} \\ |v| &= \sqrt{v_\mathrm{D}^2 + v_\mathrm{Q}^2} \\ v_\mathrm{D} \sin\theta &= v_\mathrm{Q} \cos\theta\end{aligned}$$

Here, τ_ω & τ_v represent frequency & voltage filter time constants, and k_p & k_q denote the frequency & voltage droop gains, respectively. In contrast, $|v_0|$, ω_0 & ω_b denote the nominal voltage, angular frequency setpoint & base frequency of the inverter. Furthermore, v_D & v_Q refers to the global D- and Q-axis output voltage at PCC, while i_D & i_Q refers to the global D- and Q-axis output current at PCC, respectively. θ_c denotes the PCC angle w.r.t a global DQ-frame. The reference frames are illustrated in Fig. 6.

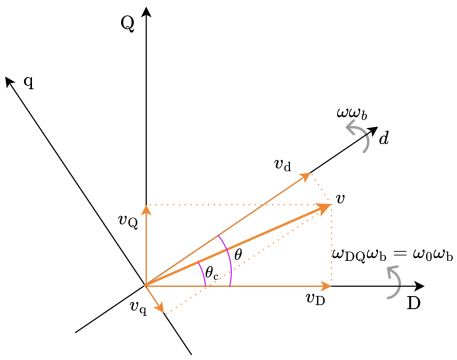

Fig. 6: Phasor diagram and reference frames of the GFM IBR.

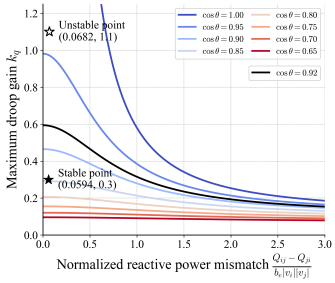

Fig. 7: Enter Caption